

Neural Network Discovery of Paired Wigner Crystals in Artificial Graphene

Conor Smith  ^{1,2} Yubo Yang (杨煜波)  ^{1,3} Zhou-Quan Wan  ¹
Yixiao Chen (陈一潇)  ⁴ Miguel A. Morales  ¹ and Shiwei Zhang  ¹

¹*Center for Computational Quantum Physics, Flatiron Institute, New York, NY, 10010, USA*

²*Department of Electrical and Computer Engineering,*

University of New Mexico, Albuquerque, NM 87131, USA

³*Department of Physics and Astronomy, Hofstra University, Hempstead, NY, 11549, USA*

⁴*ByteDance Seed*

Moiré systems have emerged as an exciting new tunable platform for engineering and probing quantum matter. A large number of exotic states have been observed, stimulating intense efforts in experiment, theory, and simulation. Utilizing a neural-network-based quantum Monte Carlo approach, we discover a new ground state of the two-dimensional electron gas in a honeycomb moiré potential at a filling factor of $\nu_m = 1/4$ (one electron every four moiré minima). In this state, two opposite-spin electrons pair to form singlet-like valence bond state which restore local C_6 symmetry in hexagonal molecules each spanning 6 moiré minima. These molecules of pairs then form a molecular Wigner crystal, leaving one quarter of the moiré minima mostly depleted. The formation of such a paired Wigner crystal, absent any confining potential or attractive interaction to facilitate “pre-assembling” the molecule, provides a fascinating case of collective phenomena in strongly interacting quantum many-body systems, and opportunities to engineer exotic properties.

Introduction

Moiré heterostructures provide a rich and versatile platform for engineering correlated quantum matter [1–6]. Their tunability has enabled the observation of a remarkable range of quantum phenomena, including generalized Wigner crystals [7–12], unconventional superconductors [13–15], and fractional quantum Hall states [16, 17]. Despite intense experimental and theoretical efforts, our understanding of their full many-body landscape remains incomplete, in part because even the best computational methods still struggle to capture emergent orders hidden in strongly correlated quantum many-body systems.

Here, we employ a neural-network quantum Monte Carlo approach [18, 19] to explore artificial graphene [20], a honeycomb moiré lattice in a two-dimensional semiconductor device, which may be realized as a layer-polarized Γ -valley transition-metal dichalcogenide (TMD) bilayer [21]. Our approach incorporates neural networks into a physically motivated variational ansatz, enabling computational discovery with a balance of strong predictive power and access to sufficiently large system sizes. Through it, we uncover an unexpected ground state:

electrons of opposite spins bind into singlet pairs with their wavefunctions spread across local hexagons, restoring C_6 symmetry. These pairs themselves crystallize into a triangular lattice, forming a genuine molecular crystal. Different from the known Wigner molecular crystals [22, 23], this state occurs at a low filling ($\nu_m = 1/4$, i.e., one electron every four moiré minima), without any confining potential or attractive interactions to drive a tendency for molecular formation. An overview of our work and illustration of the physics of the new state are presented in Fig. 1.

The state we discover is reminiscent of the paired Wigner crystal (PWC), which was proposed decades ago as a candidate ground state of the homogeneous electron gas [24, 25], but was shown to be unstable with more accurate calculations [26]. The spontaneous formation of this exotic quantum state in a moiré setting demonstrates a new route to stabilizing molecular electronic crystals. It is unexpected, not only because the state is not what conventional state-of-the-art computational methods would predict, but also because the physics is surprising. The state combines competing and seemingly incompatible elements: kinetic-energy-driven valence bond formation and pairing within each molecule, and interaction-driven Wigner crystallization of the molecular centers. Moreover, the paired state develops out of a semi-metallic phase and remains non-magnetic even deep in the insulating regime, which is contrary to expectations based on similar settings under other parameter settings (filling [27] or moiré geometry [28]) and different from what prior state-of-the-art computational methods yield, as we further discuss below. This finding not only expands the catalog of moiré phases but also illustrates the power of neural-network approaches to reveal unexpected quantum many-body phenomena. The PWC’s structure and dynamics suggest rich experimental signatures and open the door to further exotic phases such as paired super-solids.

Phase Discovery with the Neural Quantum State

Figure 1 summarizes the experimental context and the central result of this work. Figure 1(b) shows the best ground state obtained using the existing state-of-the-art approach: Diffusion Monte Carlo (DMC) projection us-

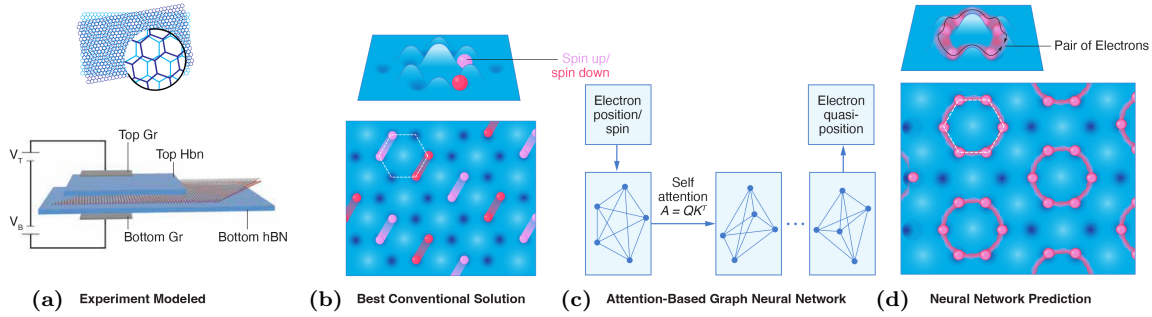


FIG. 1: Discovery of the Paired Wigner crystal state. **a**, Schematics for realization of a honeycomb lattice in a twisted TMD bilayer device. **b**, Illustration of the ground state obtained using the conventional DMC approach, which has each electron distributing over two moiré minima and forming an AFM valence bond solid. The top panel shows the landscape of the honeycomb moiré potential and electron configurations at quarter filling ($\nu_m = 1/4$). **c**, Illustration of our NQS with a backflow neural network, which transforms electron positions into quasi-positions with a self-attention graph neural network. **d**, Illustration of the NQS solution, which predicts a triangular Wigner crystal of ring motifs, each made up of a pair of up and down electrons.

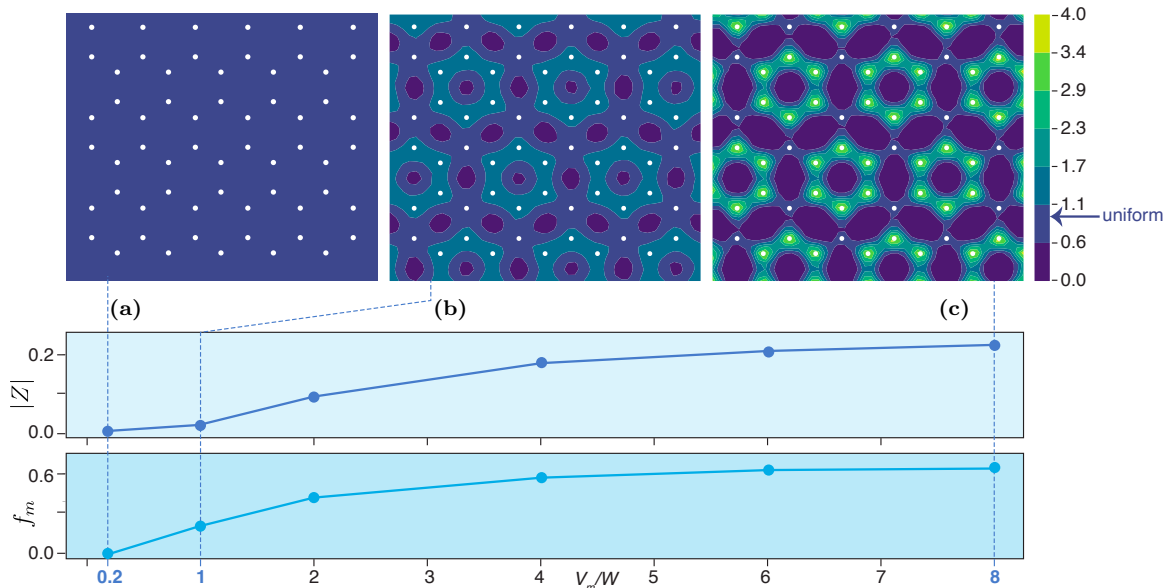


FIG. 2: Metallicity and molecular localization. **a,b,c**, The electron densities for three values of V_m/W , as indicated by the dashed lines. Metallicity is measured via the complex polarization $|Z|$, which is zero for a metal and asymptotically unity for an insulator. The molecular localization f_m measures the degree of localization on the ring motifs, characterized by the ratio of the integrated charge density inside and outside the ring. This ratio will reach unity if no electron density “leaks out of a molecule”. At low moiré potential depth, both quantities are zero, giving a metallic state with uniform density and no molecular formation. As the moiré potential deepens, both metallicity and localization become finite as the paired Wigner crystal forms.

ing an optimized Slater–Jastrow–backflow wavefunction based on orbitals derived from density-functional theory (DFT) with a hybrid functional under the local-density approximation (LDA) the details of which are in the SM. In this “conventional” solution, each electron partially occupies two neighboring moiré minima, while opposite-

spin electrons localize on far ends of a hexagonal plaquette. This configuration breaks C_6 rotation symmetry and realizes a valence-bond solid state of an antiferromagnetic insulator. In contrast, the true ground state, revealed by the NQS solution, is qualitatively different, as illustrated in Fig. 1(d). Here, opposite-spin electrons bind into sin-

glet pairs whose wavefunctions delocalize coherently over an entire hexagonal ring of six moiré minima, reminiscent of a resonating valence bond state. These singlet molecules, which fully restore C_6 symmetry, then crystallize into a triangular lattice, forming a paired Wigner crystal (PWC).

The discovery of this novel state not only underscores the power of NQS but also provides important guidance for effectively harnessing its promise. The PWC state, which is entirely missed by conventional DMC starting from mean-field orbitals, requires the flexible and expressive wavefunction representations provided by NQS. In order to confirm that the state is not an artifact of the variational ansatz, we performed a sequence of tests combining NQS with DMC, as further discussed in the SM. In brief, we use the final NQS orbitals to construct a Slater determinant, and feed the trial wavefunction derived from it into an independent DMC calculation. The PWC state remains robust in the new DMC, which yields a *lower* energy than the state obtained from the “conventional” DMC calculations pictured above in Fig. 1(b). Since DMC is variational, this indicates that the PWC state represents a genuine improvement of the nodal surface of the ground-state wave function. As NQS studies experience rapid growth, validation tests such as these will have an important role in ensuring solutions are not merely artifacts of the neural architecture and to provide increased confidence in the predictive power and relevance of this approach to experimentalists and theorists alike.

Properties

We systematically investigate the properties of the ground state as the moiré potential depth is varied. Through a number of different probes, we establish that there are at least two different phases as a function of V_m/W . At low V_m/W , the system preserves lattice translation symmetry. As V_m/W is increased, this symmetry is broken, and at sufficiently large values a molecular Wigner crystal develops, which is the state described above. In Fig. 2, panels (a-c) show the evolution of the charge density, from a nearly uniform liquid at $V_m/W = 0.2$, to weak molecular modulations at $V_m/W = 1$, and to well-formed hexagonal molecules at $V_m/W = 8$. This is illustrated further in Fig. 3(a) which shows linecuts of the charge density for a sequence of V_m/W values.

Below, we further quantify these states from several perspectives. The system is metallic at low V_m/W and the molecular Wigner crystal at large V_m/W is a PWC state. In the latter, the molecules are in a singlet, as illustrated in Fig. 3(c). Indeed, the local spin remains $S_z(\mathbf{r}) = 0$ throughout the system regardless of the moiré potential depth, as shown in Fig. 3(a). We

examine electron-electron charge and magnetic correlations. Their short-range behavior illuminates how the exchange-correlation hole of the 2DEG is influenced by the moiré potential; the long-range behavior further establishes the liquid versus crystal states. We probe the internal structure of the molecule and the intermolecular correlations in the PWC phase, which exhibit a fascinating interplay between the electron pairing and long-range order as the moiré potential depth is tuned.

Metallicity and Molecular Localization

To quantify metallicity, we calculate the complex polarization [29, 30]

$$Z = \langle \psi | \exp \left(-i \sum_{i=1}^{N_e} \mathbf{g} \cdot \mathbf{r}_i \right) | \psi \rangle, \quad (1)$$

where \mathbf{g} is the smallest reciprocal-space lattice vector commensurate with the simulation cell. In the thermodynamic limit, this quantity is 0 in a metal and $|Z| \rightarrow 1$ in an insulator. The $|Z|$ values here, which are computed in a finite simulation cell, are affected by finite-size effects and range between 0 and 1. Despite the onset of visible molecular structure at $V_m/W = 1$, $|Z|$ remains close to zero, indicating that the system remains largely delocalized. Only at $V_m/W > 1$ does $|Z|$ increase significantly, which signals a metal-insulator transition (MIT).

To quantify the degree of localization associated with molecular formation, we partition space according to those moiré minimum sites belonging to hexagonal rings with a molecule (“occupied”) and those outside (“unoccupied”). The occupancy of each moiré minimum site is defined as the integrated charge density of the Voronoi cell surrounding it

$$f_o = \frac{1}{N_o} \sum_{i \in \text{occupied}} \rho(\mathcal{V}_i) \quad (2)$$

$$f_u = \frac{1}{N_u} \sum_{i \in \text{unoccupied}} \rho(\mathcal{V}_i). \quad (3)$$

At filling $\nu_m = 1/4$, perfect molecule formation, which means all the electron densities are contained in the occupied rings with no “leakage” to the outside sites, corresponds to $f_u = 0$ and $f_o = 1/3$, whereas a uniform charge distribution yields $f_u = f_o = 1/4$. We thus define the molecular localization measure

$$f_m = 3(f_o - f_u), \quad (4)$$

which ranges from 0 for a uniform state to 1 for perfectly localized molecules. As seen in Fig. 2, f_m begins to grow already at $V_m/W = 1$, seemingly before the MIT suggested by $|Z|$. The value reaches ~ 0.6 at $V_m/W = 8$, indicating that there is still substantial “leakage” of the molecule outside the ring.

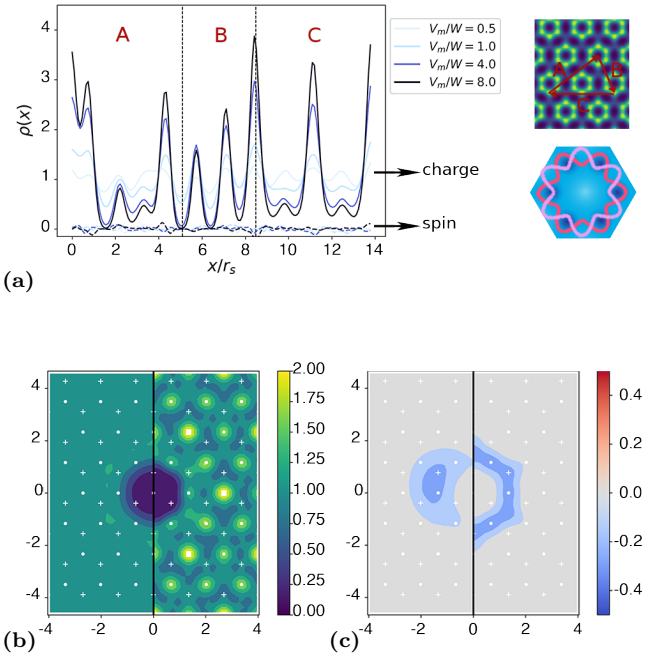


FIG. 3: Charge and spin densities and correlation functions. **a**, The charge (solid) and spin (dashed) densities are plotted along the path depicted in the top-right inset for various potential depths. The color indicates the value of V_m/W as shown in the legend box. The average charge and spin densities are indicated by the arrows. The bottom right inset shows A schematic illustration of the singlet spin state of each molecule at large V_m/W . **b**, Charge-charge correlation function with $V_m/W = 0.5$ on the left half and $V_m/W = 8.0$ on the right half; **c**, the corresponding spin-spin correlations.

Charge and Spin Correlation

Figure 3(b) contrasts the liquid and PWC phases by the charge at two representative values of the moiré potential depth. To do so, we use the charge pair correlation function, $g(\mathbf{r})$, defined as

$$g(\mathbf{r}) = \frac{1}{A} \int d\mathbf{r}' \sum_{\sigma, \sigma'} g_{\sigma, \sigma'}(\mathbf{r}, \mathbf{r} + \mathbf{r}'), \quad (5)$$

where the spin- and pair-resolved contributions are defined as

$$g_{\sigma_1, \sigma_2}(\mathbf{r}_1, \mathbf{r}_2) = \frac{\left\langle \sum_{i \neq j} \delta_{\sigma_1, \sigma_i} \delta(\mathbf{r}_1 - \mathbf{r}_i) \delta_{\sigma_2, \sigma_j} \delta(\mathbf{r}_2 - \mathbf{r}_j) \right\rangle}{\rho_{\sigma_1}(\mathbf{r}_1) \rho_{\sigma_2}(\mathbf{r}_2)}, \quad (6)$$

with $\rho_{\sigma}(\mathbf{r}) = \langle \sum_i \delta_{\sigma, \sigma_i} \delta(\mathbf{r} - \mathbf{r}_i) \rangle$. At $V_m/W = 0.5$, the behavior of $g(\mathbf{r})$ is that of a liquid, with a short-range exchange-correlation hole slightly modified by the weak moiré potential modulation. This is consistent with the

charge densities of Fig. 2(a) and Fig. 3(a) discussed earlier. At $V_m/W = 8.0$, the charge-charge correlation function exhibits long-range order consistent with a triangular lattice of molecular centers in a PWC state.

Spin correlations are studied in Fig. 3(c) for the same two systems using the spin pair correlation function

$$g_s(\mathbf{r}) = \frac{1}{A} \int d\mathbf{r}' \sum_{\sigma, \sigma'} (2\delta_{\sigma, \sigma'} - 1) g_{\sigma, \sigma'}(\mathbf{r}, \mathbf{r} + \mathbf{r}'). \quad (7)$$

As shown in Fig. 3(a), there is no net spin density anywhere. However, even in the liquid phase, the spin correlation shows a pronounced short-range pattern that breaks C_6 symmetry. This reflects the nematic spin correlation recently seen [19] in the 2DEG at intermediate density between the Wigner crystal and the high-density Fermi liquid, when the system is a correlated liquid. In the PWC phase, the spin-spin correlation function remains short-ranged, with correlations confined to distances comparable to the diameter of a single hexagonal molecule. We further examine the intra- and intermolecule spin correlations next.

Molecular Structure and Correlations of the PWC

To probe the internal structure of the singlet pairs, we first measure the angular separation between the two electrons in the same molecule. As we have seen from the charge densities, C_6 symmetry is preserved, so their angular structure can be reduced to the relative angle, as depicted in the inset in Fig. 4a. The results are shown in the main plot for a series of moiré potential depths. We see the two opposite-spin electrons tend to stay on the far ends of the same molecule ($\theta = \pi$), maximizing their separation. Configurations at nearby angular separations ($\theta = 2\pi/3, 4\pi/3$) occur with much reduced probability, while configurations in which both electrons occupy the same side of the ring ($\theta = \pi/3, 5\pi/6$) are strongly suppressed despite the presence of moiré minima there. These observations motivate a natural picture of each singlet molecule as an effective electric dipole, characterized by a center-of-mass (COM) position \mathbf{c}_i and a dipole moment \mathbf{p}_i . The dipoles are not rigidly locked to minima and can “rotate” freely to restore C_6 symmetry. As the potential depth is increased, the dipole moment increases and the structure of the dipole becomes sharper, as seen by the rise of the central peak with V_m/W .

The COMs of the molecules form a triangular lattice, as seen directly in their pair correlation function, $g(\mathbf{c}_i - \mathbf{c}_j)$, shown in Fig. 4c. To determine if the dipole moments order, we examine the alignment angle between neighboring singlets by computing $\cos(\Delta\theta) = \hat{\mathbf{p}}_i \cdot \hat{\mathbf{p}}_j$. Perfect alignment and anti-alignment of the pairs are characterized by $\Delta\theta = 0$ and π , respectively. Figure 4b shows the distribution of alignment angles for nearest neighbor singlets at several moiré depths.

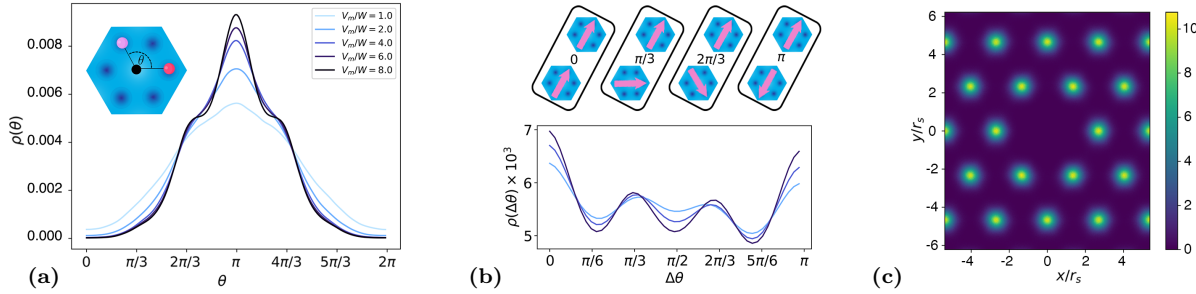


FIG. 4: Structure and correlations of the pairs. **a**, Intra-molecule correlation between the pair of up and down electrons on the same ring is characterized by the distribution of their relative angle θ , as illustrated by the inset. Curves of different colors show different moiré well depths. **b**, Orientational correlation between the nearest-neighbor pairs. The colors of the curves indicate potential well depths, as given in the legend in panel **a**. The configuration corresponding to each peak is depicted at the top of the plot. **c**, Correlation between the center-of-mass positions.

Potential Other Phases

These observations establish at least two different phases as the potential depth is tuned. Starting from the metallic liquid state at $V_m/W = 0$, pair formation and symmetry breaking occur with increasing V_m leading to a PWC with global charge localization at large moiré potential strength. In between, it is intriguing to wonder about superconductivity and the tantalizing possibility of supersolid-like behavior. This is suggested by the observation that, at $V_m/W = 1$, we see signatures of pair formation while the complex polarization remains consistent with a metallic state. We have used projected-BCS type of wave functions to conduct a preliminary exploration of this question. In our NQS-backflow ansatz, we have mostly used a determinant structure [19] but when the Slater determinant is replaced by a projected-BCS structure, the energy is further lowered. At intermediate $V_m/W \approx 4$, the largest lowering is observed as shown in Table S4. A more systematic study, with sharper detection measures and in larger system sizes, is required to address these conclusively.

Conclusion and Outlook

Using an expressive NQS tailored to perform unbiased phase discovery in strongly correlated systems, we discover a paired molecular Wigner crystal phase in a honeycomb moiré potential at $\nu_m = 1/4$. In this exotic state, opposite spin electrons form strongly correlated pairs whose charge densities delocalize over multiple moiré minima, while the resulting molecular centers crystallize into a triangular lattice. This intertwines short-range valence-bond pairing and long-range Wigner crystallization in a molecular electron solid. The state emerges in a system with purely repulsive Coulomb inter-

action and without any direct confinement for molecular formation. As such it is distinct from the rich set of states that have been seen in strongly correlated electrons.

This system is well within the realm of current experimental setups in 2D materials. Over a wide range of potential depths, we find long-range charge order together with short-range spin correlations in the form of singlet pairing. This prevalence and robustness will inspire theoretical exploration [31] and facilitate experimental detection. Given the rapid advances in experiment, including the realization of artificial graphene [20], probing of magnetism [32], and real-space imaging advances [22, 33–36] it should now be possible to search for and detect signatures of the PWC in the charge and magnetic textures.

Our results expand the landscape of correlated phases in moiré materials and suggest tantalizing new possibilities. More broadly, our findings highlight the importance of expressive and systematically improvable methods for phase discovery. The PWC state is a surprising discovery as it is different from what state-of-the-art computation would have predicted without the neural network enhancement. This motivates the further development of NQS and other many-body computation methods, and their application for predictive computations in not only moiré but other quantum platforms and materials.

ACKNOWLEDGMENTS

The Flatiron Institute is a division of the Simons Foundation. We thank Ilya Esterlis for useful discussions. YY acknowledges support by the National Science Foundation (NSF) under grant number DMR-2532734 and the use of the Hofstra Star HPC cluster, acquired with support from the NSF Major Research Instrumentation (MRI) program under grant number 2320735.

SUPPLEMENTARY INFORMATION

HAMILTONIAN

We study the ground state of holes in a semiconductor heterobilayer, a cartoon of which is shown in Fig. 1a of the main text, using the following moiré continuum Hamiltonian

$$\hat{H} = -\frac{1}{2} \sum_i \nabla_i^2 - V_m/W \sum_i \Lambda(\mathbf{r}_i) + r_s \sum_{i < j} \frac{1}{|\mathbf{r}_i - \mathbf{r}_j|}, \quad (8)$$

which assumes that the holes are confined to a single layer while the presence of the other layer can be modeled by an effective potential of the form $\Lambda(\mathbf{r}) = 2 \sum_{j=1}^3 \cos(\mathbf{r} \cdot \mathbf{g}_j + \phi)$. The vectors \mathbf{g}_j are defined as the moiré unit cell's three smallest reciprocal lattice vectors and ϕ controls the shape of the potential, which we set to $\phi = 60^\circ \pm n120^\circ$ to model the honeycomb potential realized in artificial graphene. The parameter V_m controls the depth of the moiré potential. The effective Bohr radius $a_B^* \equiv \frac{\hbar^2}{|m^*|} / \frac{e^2}{4\pi\epsilon}$ is used as length unit and the Fermi energy of the unpolarized gas $W = \frac{\hbar^2}{|m^*| r_s^2}$ is used as the energy unit. All values are given in Hartree atomic units. The Wigner-Seitz radius in Bohr units, r_s , controls the strength of Coulomb interaction relative to the kinetic energy.

THE ANSATZ

We largely use an identical ansatz as described in Ref. [19]. The main idea is to construct a determinant of orbitals built with a learnable linear combination of planewaves:

$$\phi_a(\mathbf{q}_b) = \sum_{k=1}^{N_k} c_{ak} \exp(i\mathbf{G}_k \cdot \mathbf{q}_b) \quad (9)$$

where c_{ak} is learnable and \mathbf{q}_b is a quasiposition generated by a backflow transformation as:

$$\mathbf{q}_b = \mathbf{r}_b + \mathcal{N}(\mathbf{R}) \quad (10)$$

with \mathbf{r}_b denoting the position of particle b and \mathbf{R} denoting all particle positions.

The backflow transformation is based on the message passing neural network developed in Ref. [18]. The idea is to iteratively update one-body and two-body hidden vectors, \mathbf{h}_i and \mathbf{h}_{ij} , with an attention mechanism. In more detail, the state at layer t is given by

$$\mathbf{g}_i^{(t)} = \left[\mathbf{h}_i^{(t-1)} \right], \quad \mathbf{g}_{ij}^{(t)} = \left[\mathbf{v}_{ij}, \mathbf{h}_{ij}^{(t-1)} \right] \quad (11)$$

$$\mathbf{h}_i^{(t)} = \mathcal{F}_1^{(t)} \left(\sum_{j \neq i} \mathbf{m}_{ij}^{(t)}, \mathbf{g}_i^{(t)} \right) + \mathbf{h}_i^{(t-1)}, \quad \mathbf{h}_{ij}^{(t)} = \mathcal{F}_2^{(t)} \left(\mathbf{m}_{ij}^{(t)}, \mathbf{g}_{ij}^{(t)} \right) + \mathbf{h}_{ij}^{(t-1)} \quad (12)$$

$$\mathbf{m}_{ij}^{(t)} = \mathcal{A}_{ij}^{(t)} \left(\mathbf{g}_{ij}^{(t)} \right) \odot \mathcal{F}_m^{(t)} \left(\mathbf{g}_{ij}^{(t)} \right), \quad (13)$$

where $\mathcal{F}_{h_1}^{(t)}$, $\mathcal{F}_{h_2}^{(t)}$ and $\mathcal{F}_m^{(t)}$ are multi-layer perceptrons (MLPs). The visible state \mathbf{v}_{ij} is a periodized displacement and distance vector given by,

$$\mathbf{v}_{ij} = \left[\cos(2\pi A^{-1} \mathbf{r}_{ij}), \sin(2\pi A^{-1} \mathbf{r}_{ij}), \|\sin(\pi A^{-1} \mathbf{r}_{ij})\|, \|\cos(\pi A^{-1} \mathbf{r}_{ij})\|, s_{ij} \right] \quad (14)$$

with A being the lattice vectors of the supercell and $s_{ij} = 2\delta_{\sigma_i \sigma_j - 1}$ where σ_i is the spin of particle i . The message, m_{ij} , is the element-wise multiplication of an MLP transformation of g_{ij} with an attention matrix defined as

$$\mathcal{A}_{ij}^{(t)} = \text{Linear}^{(t)} \circ \text{GELU} \left(\frac{1}{\sqrt{N}} \sum_l^N \mathbf{q}_{il}^{(t)} \mathbf{k}_{lj}^{(t)} \right), \quad (15)$$

$$\mathbf{q}_{ij}^{(t)} = W_q^{(t)} \cdot \mathbf{g}_{ij}^{(t)}, \quad \mathbf{k}_{ij}^{(t)} = W_k^{(t)} \cdot \mathbf{g}_{ij}^{(t)}. \quad (16)$$

	dimensions	layers
Iterations		3
$W_{k/q}$	32	1
\mathcal{F}_m	32	1
h_i/\mathcal{F}_1	32	2
h_{ij}/\mathcal{F}_1	26	2
\mathcal{J}	32	3

TABLE S1: Neural Network Hyperparameters

λ	1×10^{-3}
μ	0.9
η	$O(0.1)$
Decay	1000
Samples	1024

TABLE S2: Optimization Hyperparameters

To describe the backflow, we simply take the final one-body hidden state, $\mathbf{h}_i^{(L)}$, with L denoting the last layer, and apply one more MLP so that:

$$\mathcal{N}(\vec{R}) = \mathcal{F}_{bf}(\mathbf{h}_i^{(L)}). \quad (17)$$

The Jastrow is also derived from the same one-body hidden state via another MLP:

$$\mathcal{J}_\theta(\vec{R}) = \sum_i \mathcal{F}_J([\mathbf{v}_i, \mathbf{h}_i^{(L)}]). \quad (18)$$

We explicitly break translational invariance in the Jastrow by including one-body positional information, $\mathbf{v}_i = [\sin(2\pi A^{-1} \mathbf{r}_i), \cos(2\pi A^{-1} \mathbf{r}_i)]$ with A being the matrix of lattice vectors of the supercell. This choice is motivated by the fact that the moiré potential breaks continuous translational invariance (while remaining periodic).

We can compactly write the full wavefunction as

$$\Psi(\vec{r}) = \det [\{\langle \mathbf{q}_j; \sigma_j | \phi_a; \chi_a \rangle\}] \exp(\mathcal{J}_{cck}(\vec{R}) + \mathcal{J}_\theta(\vec{R})), \quad (19)$$

where orbital χ_a is an eigenstate of \hat{s}_z allowing us to write the wavefunction as product of spin- \uparrow and spin- \downarrow determinants. Finally, \mathcal{J}_{cck} is the analytical form defined by Ceperley, Chester, and Kalos [37].

OPTIMIZATION AND SAMPLING

We use the SPRING algorithm [38] to update the parameters as:

$$d\theta_t = (S + \lambda I)^{-1}(g + \lambda \mu d\theta_{t-1}) \quad (20)$$

$$\theta_{t+1} = \theta_t - \eta d\theta_t \quad (21)$$

where θ_t are the parameters of the NQS at step t , S is the quantum Fisher matrix and g are the gradients. The learning rate is given by η , λ is the damping term applied to the Fisher matrix, and $\mu > 0$ introduces a term analogous to momentum in first-order methods while $\mu = 0$ reduces to standard stochastic reconfiguration [39]. To invert the S matrix we use minSR [40, 41]. Hyperparameters are given in Table S2.

To sample from the wavefunction we use Metropolis Adjusted Langevin Algorithm [42] where samples are proposed according to:

$$\tilde{r} = r + \tau \nabla \log |\psi(r)|^2 + \sqrt{\tau} \varepsilon \quad (22)$$

and ε is randomly drawn from a Gaussian distribution. The step size, τ , is tuned adaptively to target a harmonic average of acceptance rate at 65%. We propose and accept/reject 20 updates and use only the last to calculate energies and gradients when training the wavefunction.

BCS-TYPE WAVEFUNCTION DETAILS

In this section, we present the BCS-type wavefunction referenced in the main text. We stress here that this wavefunction is not necessary to find the PWC but it does produce a lower energy than the determinant based ansatz. This is important because it is not that our work is biased to encourage pairing but rather that the apparent pairing motivated us to implement a wavefunction which can describe pairing more explicitly. To explain the form of this wavefunction, we begin with an unpaired determinant of two spin species which we can express as a product of two determinants:

$$\Psi(\vec{x}) = \left| \Phi^{(\uparrow)} \left[\vec{x}^{(\uparrow)} \right] \right| \cdot \left| \Phi^{(\downarrow)} \left[\vec{x}^{(\downarrow)} \right] \right| \quad (23)$$

where:

$$\Phi^{(\alpha)} \left[\vec{x}^{(\alpha)} \right] = \begin{bmatrix} \phi_0^{(\alpha)}(x_0) & \phi_1^{(\alpha)}(x_0) & \cdots & \phi_{N^{(\alpha)}-1}^{(\alpha)}(x_0) \\ \phi_0^{(\alpha)}(x_1) & \phi_1^{(\alpha)}(x_1) & \cdots & \phi_{N^{(\alpha)}-1}^{(\alpha)}(x_1) \\ \vdots & \vdots & \ddots & \vdots \\ \phi_0^{(\alpha)}(x_{N^{(\alpha)}-1}) & \phi_1^{(\alpha)}(x_{N^{(\alpha)}-1}) & \cdots & \phi_{N^{(\alpha)}-1}^{(\alpha)}(x_{N^{(\alpha)}-1}) \end{bmatrix}. \quad (24)$$

If $\Phi^{(\alpha)}$ is chosen to be spin-independent, the ansatz reduces to the restricted Hartree–Fock (RHF) state, which was employed in our previous simulations.

For case of $N^{(\uparrow)} = N^{(\downarrow)}$, we may alternatively employ a BCS-like wave function of the form $|\Psi_{\text{bcs}}\rangle = (F_{kk'}c_{k\uparrow}^\dagger c_{k'\downarrow}^\dagger)^{N/2}$, where F is the pairing matrix and c_k^\dagger creates an electron in the plane-wave basis. In practice, however, the dimension of the plane-wave basis is much larger than the number of electrons, rendering a full parameterization of the pairing matrix F_{ij} inefficient. To reduce the number of variational parameters, we first construct a reduced set of $n_{\text{orb}} > N/2$ single-particle orbitals from the plane-wave basis, $c_{i\alpha}^\dagger = \sum_{\vec{k}} A_{i,\vec{k}}^\alpha c_{\vec{k}}^\dagger$, where i labels the orbital index and A^α are variational orbital-parameter matrices. The BCS-like wave function can then be written as $|\Psi_{\text{bcs}}\rangle = (\sum_i S_i c_{i\uparrow}^\dagger c_{i\downarrow}^\dagger)^{N/2}$, where S_i are diagonal pairing parameters. This form is sufficient because any non-diagonal structure of the pairing matrix can be absorbed into the orbital rotations encoded in A^α , leaving only the diagonal pairing amplitudes S_i as independent variational parameters. In our simulations, we typically choose the orbital dimension to be $n_{\text{orb}} = N^\uparrow + N^\downarrow$.

To be more explicit, in real-space coordinates \vec{x} the BCS-like wave function can be evaluated as

$$\Psi(\vec{x}) = \det \left[\Phi^{(\uparrow)} \left[\vec{x}^{(\uparrow)} \right] S(\Phi^{(\downarrow)} \left[\vec{x}^{(\downarrow)} \right])^T \right], \quad (25)$$

where $\Phi^\alpha \in \mathbb{C}^{N^\alpha, n_{\text{orb}}}$ are the spin-resolved orbital matrices, defined as in Eq. (24) but with an enlarged orbital dimension $n_{\text{orb}} > N^\alpha$.

Both the standard form in Eq. 23 and the BCS form identify the PWC as the lowest-energy state. However, the BCS wave function consistently yields a lower variational energy. A detailed comparison of the energies is presented in Table S4 where we also include the energy of the fully polarized system to illustrate the energy lowering from pairing electrons in singlets. To better illustrate the structure encoded by the BCS wave function, we compute the occupation amplitudes, defined as the singular values of the effective pairing matrix in the present parameterization, $F \equiv A^{(\downarrow)T} S A^{(\uparrow)}$. These occupation amplitudes generally differ from the diagonal matrix S because no orthogonality constraint is imposed on the orbital operators $c_{i,\alpha}^\dagger$. In Fig. S1, we plot the occupation amplitudes for different values of V_m/W . For $V_m/W = 0.1$, where the ground state is expected to be well captured by an RHF-like wave function, the occupation amplitudes exhibit a sharp drop at the $N/2$ -th largest value, indicating that the state effectively reduces to an RHF state. As V_m/W is increased and the paired Wigner crystal phase emerges, the occupation amplitudes display qualitatively different behavior compared to the $V_m/W = 0.1$. In particular, the tail of the occupation spectrum persists and becomes increasingly pronounced with increasing V_m/W . This behavior provides evidence that the pairing mechanism encoded in the BCS wave function plays an essential role in stabilizing the paired Wigner crystal phase, consistent with the observed lowering of the variational energy.

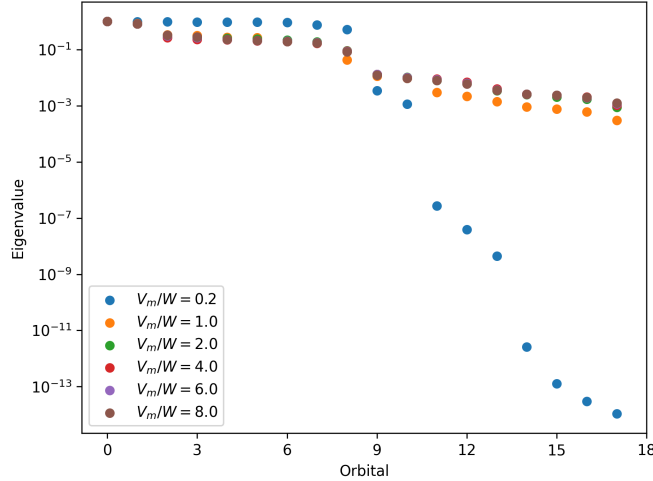


FIG. S1: Eigenvalues of orbitals in the projected-BCS wavefunction

COMPARING ENERGIES OF CANDIDATE GROUND STATES

It is always possible that there is a state lower in energy that is qualitatively different than the PWC. However, in this section we provide more evidence supporting the fact that it is the ground state by comparing with various candidate states and providing energies from DMC.

	Mean
NN-VMC	-2.2865(2)
NN-BCS-VMC	-2.2999(2)
LDA-DMC	-2.2991(6)
NNOrb-DMC	-2.3007(2)

TABLE S3: Energies for $V_m/W = 2$ comparing Variational Monte Carlo with Neural Network backflow to DMC with orbitals of LDA, Slater-Jastrow and those found by the neural network.

In Table S3, we compare the energies obtained with the neural network with and without the BCS determinant to those obtained with DMC. The LDA orbitals do not find the PWC but find comparable energies to the BCS (MP)²NQS when the LDA orbitals are used in a DMC calculation. To ensure that the PWC we find is not explicitly the result of a bias in our ansatz, we test DMC with orbitals obtained from the (MP)²NQS. Both cases are lower than LDA-DMC and lower than the (MP)²NQS and find the PWC and so we are confident this is not a result of a bias in the optimization of our ansatz. It is likely that if we run DMC on the full network and orbitals, the energy will lower more but that is left for future work.

	$V_m/W = 2.0$	$V_m/W = 4.0$	$V_m/W = 6.0$	$V_m/W = 8.0$
NN-P	-1.77211(6)	-2.2833(2)	-2.88069(7)	-3.53534(9)
NN-UP	-1.7910(1)	-2.2865(2)	-2.8882(2)	-3.5482(2)
NN-BCS-UP	-1.7953(4)	-2.2999(2)	-2.8955(5)	-3.5515(2)

TABLE S4: Ground state energies comparing Variational Monte Carlo with Neural Network backflow for the polarized system, the unpolarized system with a standard determinant and the unpolarized with a BCS type determinant.

PAIRED WIGNER CRYSTAL IN DIFFERENT LATTICES, GEOMETRIES AND DENSITIES

To check that the PWC is not an artifact of cell size or shape, we show various system sizes and compare the triangular cell to the rectangular cell. All cases utilize the same filling of $\nu = 1/4$. This corresponds to 8 electrons on the 4×4 lattice, 18 electrons on the 6×6 lattice, 32 electrons on the 8×8 lattice and 24 electrons on the 6×8 lattice. From the charge density plots in Fig. S2 it is clear that the PWC is robust from a 4×4 lattice to an 8×8 lattice and in triangular as well as rectangular cells.

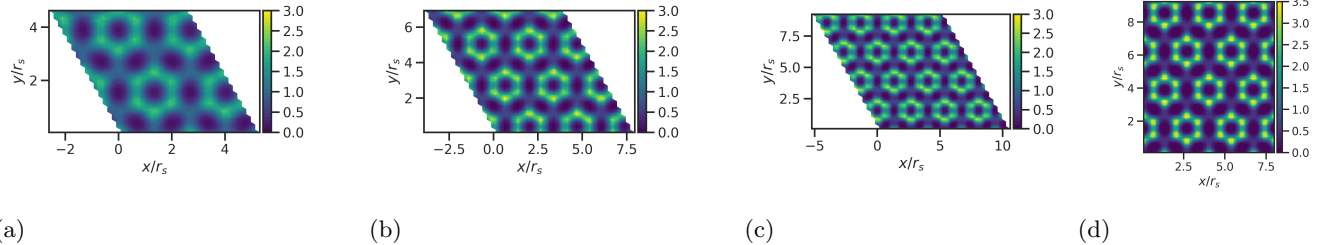


FIG. S2: Ground state charge densities are shown for $r_s = 10$ with lattice sizes and potential depths of (a) 4×4 , $V_m/W = 2.0$, (b) 6×6 , $V_m/W = 4.0$, (c) 8×8 , $V_m/W = 6.0$ and (d) 6×8 , $V_m/W = 8.0$. All simulations are done at the same filling, $\nu = 1/4$, as in the main text. (a-c) are in a triangular cell while (d) is in a rectangular cell.

To show that this phase is robust over a region accessible by various experimental devices, we also include here the result at $r_s = 5$ and $r_s = 15$ whereas the results in the main text are strictly at $r_s = 10$. In Fig. S3 we show charge densities at $V_m/W = 2.0$ for $r_s = 5$ and $r_s = 15$. Both systems are on a 6×6 lattice with 18 electrons and exhibit the same hexagonal PWC pattern. In sum, this gives us confidence that the phase is robust to cell shape, is not a finite size effect and is stable over a density of at least $r_s = 5$ to $r_s = 15$.

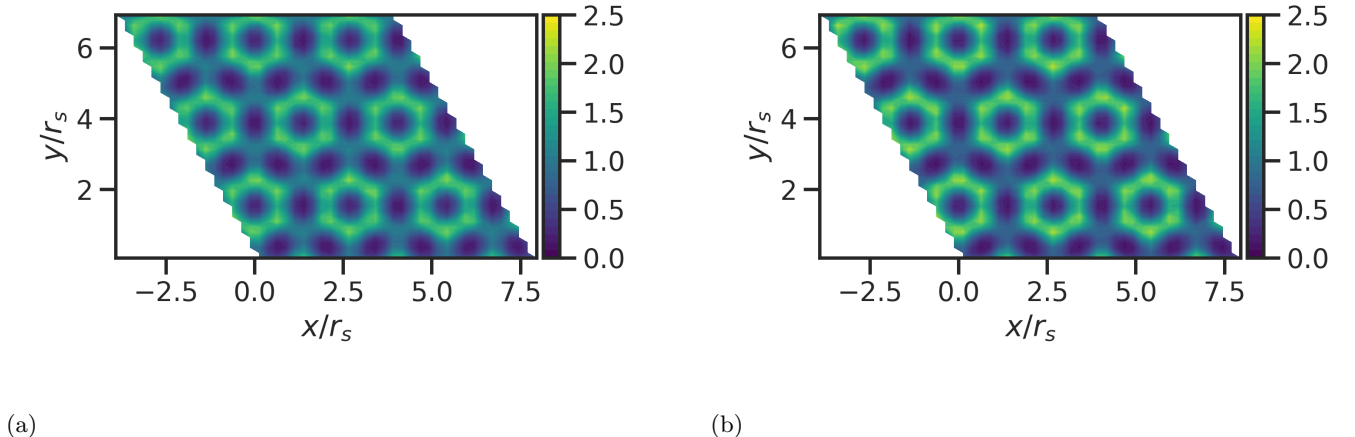


FIG. S3: Ground state charge densities are shown for $V_m = 2.0$ at $r_s = 5$ in (a) and $r_s = 15$ in (b). Both simulations are done at the same filling, $\nu = 1/4$, as in the main text in a triangular cell on a 6×6 lattice.

DESCRIPTIONS OF THE DENSITY FUNCTIONAL THEORY AND DIFFUSION MONTE CARLO CALCULATIONS

In addition to the NQS calculations, we also looked for solutions of the moiré continuum Hamiltonian Eq. (8) using traditional electronic structure methods including density functional theory (DFT) and diffusion Monte Carlo (DMC). The numerical details are consistent with those in Refs. [27, 28], but with the system modified to match that explored by the NQS calculations: 18 electrons in 36 moiré unit cells with periodic boundary conditions.

We were unable to locate the ring state using DFT. As shown in Fig. S4, LDA predicts a gapless ferromagnetic ground state starting in moderately deep moiré potential $V_M/W \geq 1$ which persists in deeper potentials. The introduction of exact exchange into LDA stabilizes an anti-ferromagnetic state. However, instead of singlets that span hexagonal rings, this state can be viewed as two staggered triangular lattices, one formed by up spins, while the other by down spins. As shown in Fig. S5, each electron is delocalized across two moiré minima, forming a “bowtie” pattern. Opposite-spin electrons occupy opposing edges of what would have been honeycomb rings from the NQS calculation. As such, this state can be viewed as the “closest” mean-field solution that approximates the paired Wigner crystal.

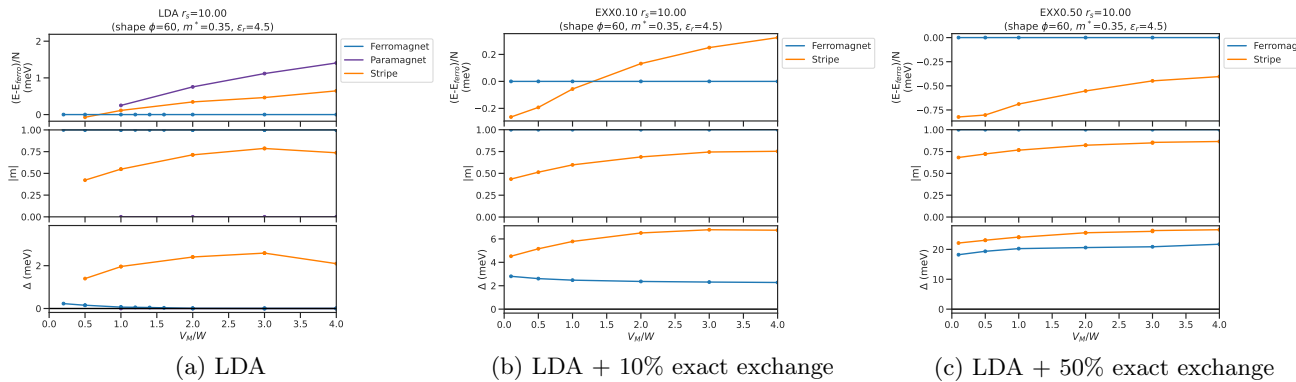


FIG. S4: DFT energy, magnetization, and gap as functions of the depth of the moiré potential at $r_s = 10$.

To obtain the energies presented in Table S3, we performed DMC calculations using Slater-Jastrow trial wavefunctions using LDA and neural-network orbitals. For each set of orbitals, we optimized short-range two-body Jastrows and used the resultant trial wavefunctions in subsequent DMC calculations with timesteps of 0.25 ha^{-1} , which resulted in an acceptance ratio of 99.8%. We used 1024 walkers, which is more than sufficient for this small system of $N = 36$ electrons.

[1] D. M. Kennes, M. Claassen, L. Xian, A. Georges, A. J. Millis, J. Hone, C. R. Dean, D. N. Basov, A. N. Pasupathy, and A. Rubio, *Nat. Phys.* **17**, 155 (2021).

[2] K. F. Mak and J. Shan, *Nat. Nanotechnol.* **17**, 686 (2022).

[3] P. C. Adak, S. Sinha, A. Agarwal, and M. M. Deshmukh, *Nat Rev Mater* **9**, 481 (2024).

[4] E. Y. Andrei, D. K. Efetov, P. Jarillo-Herrero, A. H. MacDonald, K. F. Mak, T. Senthil, E. Tutuc, A. Yazdani, and A. F. Young, *Nat Rev Mater* **6**, 201 (2021).

[5] J. G. Checkelsky, B. A. Bernevig, P. Coleman, Q. Si, and S. Paschen, *Nat Rev Mater* **9**, 509 (2024).

[6] K. P. Nuckolls and A. Yazdani, *Nat Rev Mater* **9**, 460 (2024).

[7] L. Wang, E.-M. Shih, A. Ghiotto, L. Xian, D. A. Rhodes, C. Tan, M. Claassen, D. M. Kennes, Y. Bai, B. Kim, K. Watanabe, T. Taniguchi, X. Zhu, J. Hone, A. Rubio, A. N. Pasupathy, and C. R. Dean, *Nature Materials* **19**, 861 (2020).

[8] E. C. Regan, D. Wang, C. Jin, M. I. Bakti Utama, B. Gao, X. Wei, S. Zhao, W. Zhao, Z. Zhang, K. Yu-migeta, M. Blei, J. D. Carlström, K. Watanabe, T. Taniguchi, S. Tongay, M. Crommie, A. Zettl, and F. Wang, *Nature* **579**, 359 (2020).

[9] T. Li, S. Jiang, L. Li, Y. Zhang, K. Kang, J. Zhu, K. Watanabe, T. Taniguchi, D. Chowdhury, L. Fu, J. Shan, and K. F. Mak, *Nature* **597**, 350 (2021), 2103.09779.

[10] S. Shabani, D. Halbertal, W. Wu, M. Chen, S. Liu, J. Hone, W. Yao, D. N. Basov, X. Zhu, and A. N. Pasupathy, *Nature Physics* **17**, 720 (2021).

[11] R. Nielen, A. Roche, F. Mahdikhanyarvejehany, T. Taniguchi, K. Watanabe, M. R. Koehler, D. G. Mandrus, J. Schaibley, and B. J. LeRoy, *APL Materials* **10**, 031107 (2022).

[12] Y. Zhou, I. Esterlis, and T. Smoleński, *arXiv e-prints*, arXiv:2509.21222 (2025), arXiv:2509.21222 [cond-mat.str-el].

[13] Y. Xia, Z. Han, K. Watanabe, T. Taniguchi, J. Shan, and K. F. Mak, *Nature* **637**, 833 (2025).

[14] Y. Guo, J. Pack, J. Swann, L. Holtzman, M. Cothrine, K. Watanabe, T. Taniguchi, D. G. Mandrus, K. Barmak, J. Hone, A. J. Millis, A. Pasupathy, and C. R. Dean, *Nature* **637**, 839 (2025).

[15] Y. Jia, T. Song, Z. J. Zheng, G. Cheng, A. J. Uzan,

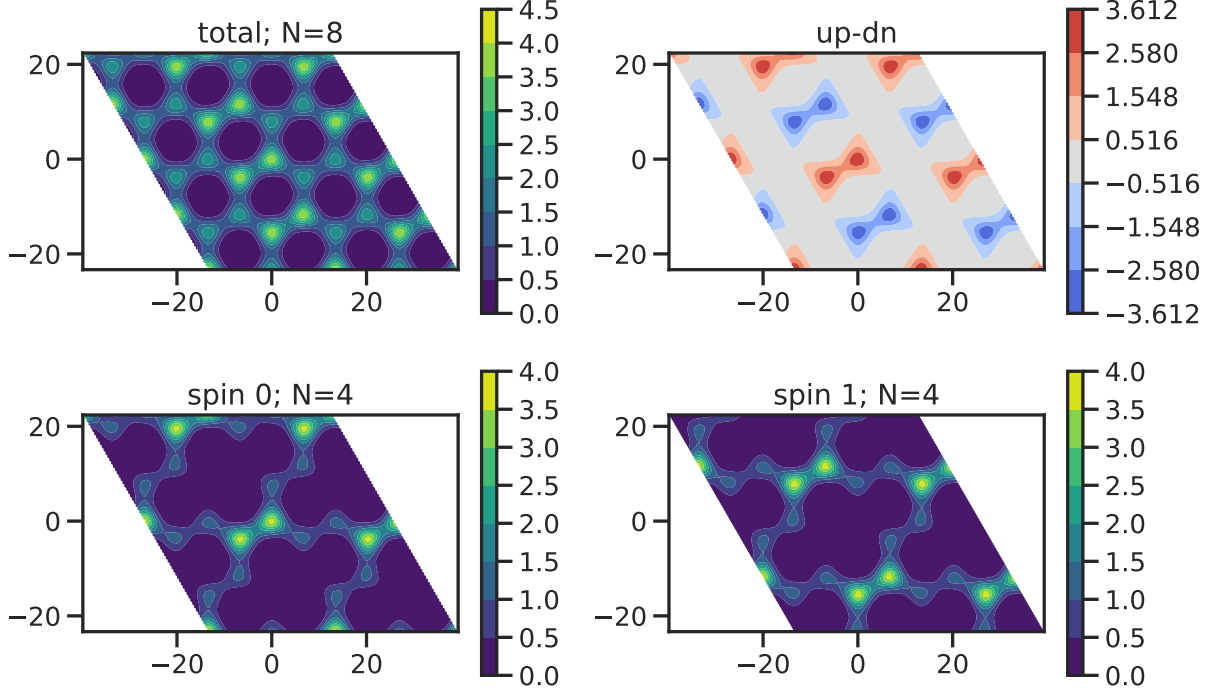


FIG. S5: Charge and spin densities of the antiferromagnetic DFT state that best approximates the paired Wigner crystal.

G. Yu, Y. Tang, C. J. Pollak, F. Yuan, M. Onyszczak, K. Watanabe, T. Taniguchi, S. Lei, N. Yao, L. M. Schoop, N. P. Ong, and S. Wu, *Sci. Adv.* **11**, eadq5712 (2025).

[16] J. Cai, E. Anderson, C. Wang, X. Zhang, X. Liu, W. Holtzmann, Y. Zhang, F. Fan, T. Taniguchi, K. Watanabe, Y. Ran, T. Cao, L. Fu, D. Xiao, W. Yao, and X. Xu, *Nature* **622**, 63 (2023).

[17] C. Wang, X.-W. Zhang, X. Liu, Y. He, X. Xu, Y. Ran, T. Cao, and D. Xiao, *Physical Review Letters* **132**, 036501 (2024).

[18] G. Pescia, J. Nys, J. Kim, A. Lovato, and G. Carleo, *Phys. Rev. B* **110**, 035108 (2024).

[19] C. Smith, Y. Chen, R. Levy, Y. Yang, M. A. Morales, and S. Zhang, *Physical Review Letters* **133**, 10.1103/physrevlett.133.266504 (2024).

[20] L. Ma, R. Chaturvedi, P. X. Nguyen, K. Watanabe, T. Taniguchi, K. F. Mak, and J. Shan, *arXiv e-prints*, arXiv:2412.07150 (2024), arXiv:2412.07150 [cond-mat.mes-hall].

[21] M. Angeli and A. H. MacDonald, *Proceedings of the National Academy of Sciences* **118**, 1 (2021).

[22] H. Li, Z. Xiang, A. P. Reddy, T. Devakul, R. Sailus, R. Banerjee, T. Taniguchi, K. Watanabe, S. Tongay, A. Zettl, L. Fu, M. F. Crommie, and F. Wang, *Science* **385**, 86 (2024).

[23] X. Li, Y. Qian, W. Ren, Y. Xu, and J. Chen, *Emergent wigner phases in moiré superlattice from deep learning* (2024), arXiv:2406.11134 [physics.comp-ph].

[24] K. Moulopoulos and N. W. Ashcroft, *Phys. Rev. Lett.* **69**, 2555 (1992).

[25] M. Taut, *Phys. Rev. B* **64**, 165315 (2001).

[26] N. D. Drummond and R. J. Needs, *Phys. Rev. Lett.* **102**, 126402 (2009).

[27] Y. Yang, M. A. Morales, and S. Zhang, *Phys. Rev. Lett.* **133**, 266501 (2024).

[28] Y. Yang, M. A. Morales, and S. Zhang, *Phys. Rev. Lett.* **132**, 076503 (2024).

[29] R. Resta and S. Sorella, *Phys. Rev. Lett.* **82**, 370 (1999).

[30] I. Souza, T. Wilkens, and R. M. Martin, *Phys. Rev. B* **62**, 1666 (2000).

[31] D. Zverevich, A. Levchenko, and I. Esterlis, *arXiv e-prints*, arXiv:2601.05318 (2026), arXiv:2601.05318 [cond-mat.str-el].

[32] Y. Tang, K. Su, L. Li, Y. Xu, S. Liu, K. Watanabe, T. Taniguchi, J. Hone, C.-M. Jian, C. Xu, K. F. Mak, and J. Shan, *Nat. Nanotechnol.* **18**, 233 (2023).

[33] Y.-C. Tsui, M. He, Y. Hu, E. Lake, T. Wang, K. Watanabe, T. Taniguchi, M. P. Zaletel, and A. Yazdani, *Nature* **628**, 287 (2024).

[34] Z. Xiang, H. Li, J. Xiao, M. H. Naik, Z. Ge, Z. He, S. Chen, J. Nie, S. Li, Y. Jiang, R. Sailus, R. Banerjee, T. Taniguchi, K. Watanabe, S. Tongay, S. G. Louie, M. F. Crommie, and F. Wang, *Science* **388**, 736 (2025).

[35] Z. Ge, C. Smith, Z. He, Y. Yang, Q. Li, Z. Xiang, J. Xiao, W. Zhou, S. Kahn, M. Erdi, R. Banerjee, T. Taniguchi, K. Watanabe, S. A. Tongay, M. A. Morales, S. Zhang, F. Wang, and M. F. Crommie, *Visualizing the Impact of Quenched Disorder on 2D Electron Wigner Solids* (2025).

[36] E. Berger, M. Arumainayagam, Z. Dong, L. Schneider, T. Wang, G. Nichols, S. Kahn, R. Dutta, G. Wang, T. Taniguchi, K. Watanabe, M. H. Naik, M. P. Zaletel, F. Wang, and M. F. Crommie, *Imaging Electron-Hole Asymmetry in the Quantum Melting of Generalized Wigner Crystals* (2025).

[37] D. M. Ceperley, G. V. Chester, and M. H. Kalos, *Phys. Rev. D* **13**, 3208 (1976).

- [38] G. Goldshlager, N. Abrahamsen, and L. Lin, *Journal of Computational Physics* **516**, 113351 (2024).
- [39] S. Sorella, *Physical Review Letters* **80**, 4558–4561 (1998).
- [40] Y. Chen, H. Xie, and H. Wang, Efficient numerical algorithm for large-scale damped natural gradient descent (2023), arXiv:2310.17556 [cs.LG].
- [41] A. Chen and M. Heyl, *Nature Physics* **20**, 1476–1481 (2024).
- [42] J. Besag, *J. Roy. Statist. Soc. Ser. B* **56**, 4 (1994).